

ORIGINAL RESEARCH ARTICLE

Influence of Y_2O_3 reinforcement particles during heat treatment of IN718 composite produced by laser powder bed fusion

Duy Nghia Luu¹, Wei Zhou^{1,2*}, Sharon Mui Ling Nai^{3*}

¹School of Mechanical and Aerospace Engineering, Nanyang Technological University, 50 Nanyang Avenue, Singapore 639798, Singapore

²Singapore Centre for 3D Printing, School of Mechanical and Aerospace Engineering, Nanyang Technological University, 50 Nanyang Avenue, Singapore 639798, Singapore

³Singapore Institute of Manufacturing Technology (SIMTech), Agency for Science, Technology and Research (A*STAR), Additive Manufacturing Division, 5 Cleantech Loop, CleanTech Two Block B, Singapore 636732, Singapore

Abstract

A metal matrix composite with Inconel 718 as the base metal and yttrium oxide (Y_2O_3) as the reinforcement particles was fabricated by the laser powder bed fusion technology. This paper presents a comprehensive study on the influence of the Y_2O_3 reinforcement particles on the microstructures and mechanical properties of the heat-treated printed composite. Complex precipitates formation between the Y_2O_3 nanoparticles and the carbonitride precipitates were shown. The complex precipitates separated into individual Y_2O_3 and titanium nitride (TiN) nanoparticles after heat treatment. Nano-sized Y-Ti-O precipitates were observed after solutionization due to the release of supersaturated Y in the metal matrix. Grain refinement was also observed in the heat-treated composites due to the high number of nano-sized precipitates. After solutionizing and aging, the grain size of the Y_2O_3 -reinforced sample is 28.2% and 33.9% smaller, respectively, than that of the monolithic Inconel 718 sample. This effectively reduced the segregation of Nb at the grain boundaries and thus, γ' and γ'' precipitates were distributed in the metal matrix more homogeneously. Combined with the increased Orowan strengthening from a significantly higher number of nano-sized precipitates and grain boundary strengthening, the composite achieved higher yield strength, and ultimate tensile strength (1099.3 MPa and 1385.5 MPa, respectively) than those of the monolithic Inconel 718 (1015.5 MPa and 1284.3 MPa, respectively).

***Corresponding authors:**

Wei Zhou
(mwzhou@ntu.edu.sg)
Sharon Mui Ling Nai
(mlnai@simtech.a-star.edu.sg)

Citation: Luu DN, Zhou W, Nai SML, 2022, Influence of Y_2O_3 reinforcement particles during heat treatment of IN718 composite produced by laser powder bed fusion. *Mater Sci Add Manuf*, 1(4): 25.

<https://doi.org/10.18063/msam.v1i4.25>

Received: October 10, 2022

Accepted: December 7, 2022

Published Online: December 22, 2022

Copyright: © 2022 Author(s). This is an Open Access article distributed under the terms of the Creative Commons Attribution License, permitting distribution, and reproduction in any medium, provided the original work is properly cited.

Publisher's Note: AccScience Publishing remains neutral with regard to jurisdictional claims in published maps and institutional affiliations.

Keywords: Laser powder bed fusion; Additive manufacturing; Inconel 718; Y_2O_3 reinforcement; Heat treatment

1. Introduction

Fabricating metalmatrix composites (MMCs) with discontinuous reinforcements have been steadily gaining interest over the years to improve existing materials and tackle new challenges. The MMCs usually have high modulus, strength, and stiffness, good fatigue properties, and high-temperature performance^[1,2]. This is made possible due to the exceptional ability of the MMCs to combine the ductile and tough characteristics of

metals with the wear resistance, stiffness, and rigidness of ceramic materials. One of the prime material candidates to be used as the base metal is Inconel 718 (IN718) due to its excellent strength, ductility, and creep resistance at high temperatures^[3]. Thus, the material is in high demand in the aerospace industry, presenting the need to further enhance its mechanical properties to widen its industry applications.

The traditional manufacturing methods for MMCs can be categorized into either solid-state or liquid-state methods^[4]. For solid-state methods, the alloying of individual components takes place by repeatedly welding and fracturing the raw powder, which takes a very long time to complete. Friction stir processing (FSP) is another promising solid-state method that is able to produce MMCs. However, this method is primarily used to produce surface composites^[5,6] and requires extensive process optimization and simulation to understand the effects of those parameters on the homogeneity of the composite^[7]. Liquid-state methods usually involve different ways of introducing the reinforcement particles into the liquid melt^[8]. This can be done by simply adding the reinforcement particles into a molten metal followed by mechanical agitation such as stirring. The primary problems are to ensure the homogeneous dispersion of the particles within the liquid melt as well as to ensure good wettability between the reinforcement and the matrix, which can be challenging^[9]. On the other hand, the liquid melt can also be infiltrated into a ceramic preform to manufacture MMCs^[10]. However, the properties of the MMCs manufactured by this method depend on the characteristics of the preform, which requires monitoring the size, shape, and interconnectedness of the pores or cells. As such, it is often substantially complex and expensive to design and manufacture the preform^[11].

It should also be noted that the final product from the traditional manufacturing methods usually has simple forms such as tube, sheet, or ingot. Due to the high strength of IN718, it is difficult and costly to produce complex parts from those simple forms. Fortunately, due to the excellent weldability of IN718, the material and its composites are suitable to be fabricated by additive manufacturing (AM), a method that has revolutionized the traditional manufacturing industry. In this study, laser powder bed fusion (LPBF) is utilized to fabricate IN718 MMCs to overcome the drawbacks of traditional manufacturing methods. For instance, the technology is well known for its ability to produce near-net shape products. Furthermore, homogeneously dispersed reinforcement particles could be achieved using the technology by making use of its short melt-pool lifetime and high cooling rate. However,

despite the advantages of using AM for IN718 MMCs, the development of printed IN718 MMCs is quite recent and only limited to a few groups of researchers^[12-15].

One of the most commonly used types of reinforcements is oxides due to several of their outstanding properties^[16]. This paper presents a comprehensive microstructural and mechanical property study of the IN718 MMC reinforced with yttrium oxide (Y_2O_3). The study was done in heat-treated MMC because IN718 must be heat treated to make use of its precipitation hardening characteristic. Thus, it is of utmost importance to understand the effect of the reinforcement particles on the different phases in IN718. Unfortunately, studies regarding the heat-treated IN718/ Y_2O_3 material system have not been presented. There are only a handful of studies related to the heat treatment of oxide-reinforced Ni-based alloys^[17,18] while most of the studies are for Fe-based alloys^[19-21]. As such, this study will provide a comprehensive comparison of the microstructures and mechanical properties between the Y_2O_3 -reinforced IN718 Ni-based alloys and the monolithic IN718 in the as-printed state as well as after each stage of the heat treatment. This study also showed the importance of heat treatment to the Y_2O_3 -reinforced IN718 as the value added of the Y_2O_3 nanoparticles could not be showcased in the as-printed state.

2. Methods and materials

2.1. Powder preparation and LPBF process

Commercially available IN718 powder (20 – 63 μm) was purchased from Höganäs. The chemical compositions of the powder are listed in Table 1. The scanning electron microscopy (SEM) images of the IN718 and nano- Y_2O_3 (30 – 100 nm) powder are shown in Figure 1A and B, respectively.

The reinforcement particles were mixed with the IN718 powder using the Inversina 20L tumbler mixer for 8 h. The amount of reinforcement particles was 1 wt.%. Steel balls were added with a 1 – 3, ball-to-powder, ratio during mixing to enhance the dispersion homogeneity. A uniform mixture of powder was obtained as shown in Figure 1C. It can be seen that the Y_2O_3 particles were able to attach themselves to the surface of the IN718 powder particles.

The time needed for a homogeneous powder mixture was first determined visually using a camera by observing the mixture after 2, 4, 6, and 8 h of mixing as shown in Figure 2A-D. It was observed that the white Y_2O_3 nanoparticles were still agglomerated after 2 h of mixing. As the mixing time increased, the nanoparticles were distributed more homogeneously in the mixture, and they were no longer in large clusters after 6 h and were fully

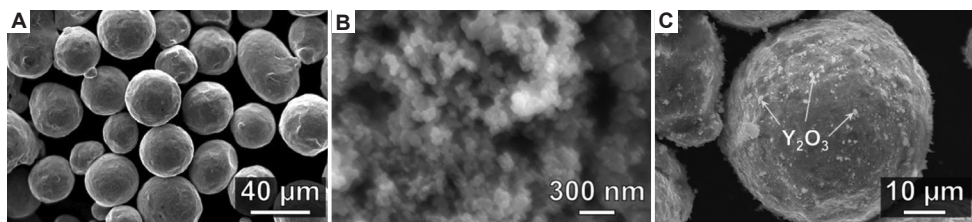


Figure 1. Scanning electron microscopy (SEM) images of IN718 (A) and nano-Y₂O₃ (B). SEM image of IN718 mixed with nano-Y₂O₃ (C).

Table 1. Chemical compositions (wt.%) of IN718 powder

| Ti | Nb | Mo | Cr | C | B | P | Ni | Fe | O | N | Si | S | Mn | Al | Co |
|------|------|------|------|------|-------|-------|----|------|------|------|------|-------|------|------|------|
| 0.73 | 5.33 | 3.03 | 18.6 | 0.01 | 0.014 | 0.002 | 54 | Bal. | 0.03 | 0.16 | 0.51 | 0.002 | 0.18 | 0.39 | 0.02 |

blended with the IN718 powder after 8 h. The resultant homogeneously mixed powder was then examined under SEM. The white Y₂O₃ nanoparticles were observed on the surface of all the IN718 powder particles as shown in [Figure 2E](#). The chemical compositions of the white nanoparticles at 15 distinct locations were analyzed using energy dispersive X-ray (EDX) and the average wt.% of the major elements is listed in [Table 2](#). The presence of Y and O was detected, further confirming the nanoparticles to be Y₂O₃.

The samples were printed using the ProX300 machine (3D Systems) using 50 μm hatch spacing and 40 μm layer thickness. As referenced from our previous works^[22,23], after extensive process parameters optimization, the optimal laser power and scan speed are listed in [Table 3](#). A fiber laser, with a 1070 nm wavelength and 75 μm spot size, was used. An island printing strategy was employed, with each island being a hexagon with a 25000 μm radius. The scanning tracks were rotated 90° for each consecutive layer.

2.2. Heat treatment profiles

All the samples were solutionized and aged in a vacuum tube furnace (Lenton, UK). The solutionizing treatment for tensile specimens was carried out at 1075°C at a heating up rate of 15°C/min, held for 1 h, followed by furnace cooling at a rate of 10°C/min. The aging treatment of the samples was also carried out in a vacuum tube furnace at a heating rate of 10°C/min to 720°C, held for 8 h, followed by furnace cooling at a rate of 10°C/min to 620°C, held for another 8 h, followed by furnace cooling at a rate of 10°C/min to room temperature. This aging treatment profile is similar to the one used in other studies^[24-27].

However, to understand the reasons behind the differences in the mechanical properties of the samples after aging treatment, all the samples were also subjected to solutionizing treatment at 1275°C using the same heating

Table 2. Chemical compositions (wt.%) of the white nanoparticles in the powder mixture after 8 h of mixing

| O | Cr | Fe | Ni | Y |
|-----------|------------|------------|------------|-----------|
| 5.46±1.54 | 19.06±1.08 | 17.61±0.79 | 47.95±1.87 | 9.91±1.51 |

Table 3. Laser power and scan speed for the LPBF process of IN718 samples

| Reinforcement | Laser power (W) | Scan speed (mm/s) |
|--------------------------------------|-----------------|-------------------|
| Nil | 238 | 1000 |
| 1 wt.% Y ₂ O ₃ | 260 | 1000 |

rate, holding time, and cooling rate as the solutionizing treatment at 1075°C before aging. The percentage of the area occupied by the γ' and γ'' precipitates is calculated using the ImageJ software. The samples are labeled as shown in [Table 4](#). The heat treatment profiles are shown in [Figure 3](#).

2.3. Material characterization

The samples were ground and polished along the building direction using the typical procedure. Microstructural analysis was carried out after the samples were etched with Kalling's No. 2 reagent. The SEM of the Y₂O₃ sample was prepared by dispersing the powder in ethanol and drop-cast into a Si substrate. Imaging and energy dispersive X-ray (EDX) analyses were carried out using the field emission scanning electron microscope (FESEM) JEOL-JSM-7600F and the Ultra Plus FESEM from Carl Zeiss FESEM machines. The printed samples were wire-cut into tensile coupons with dimensions with a gauge length of 14 mm as shown in [Figure 4](#). Tensile testing was carried out using the INSTRON 5982 machine, at a strain rate of 0.01/s at room temperature. The tensile direction was perpendicular to the building direction. The chosen dimensions and processing parameters of the tensile coupons would result

in comparable or better mechanical properties than those reported by other literature as shown in our previous study Luu *et al.*^[22].

The grain size was calculated using the line intersection method. The width and length of the grains would then be

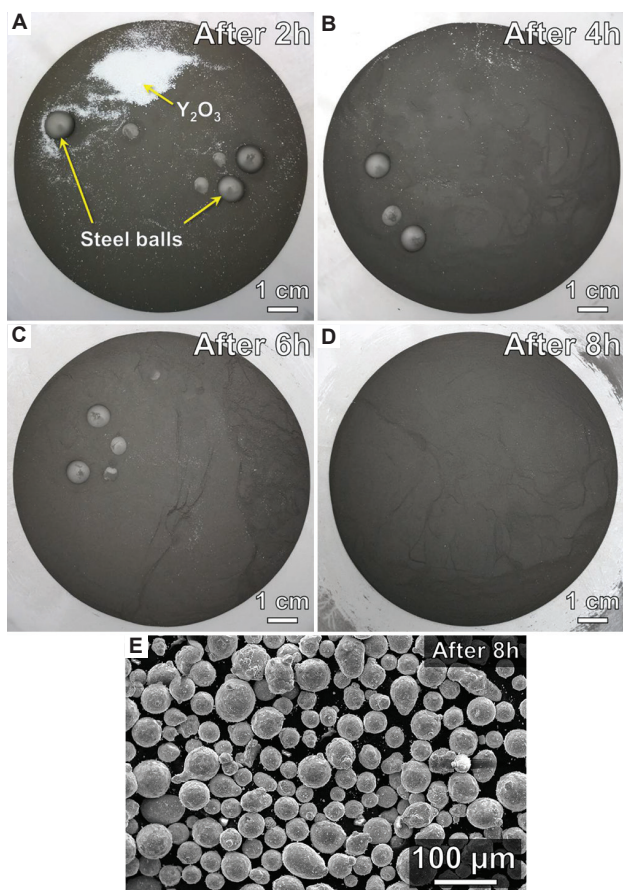


Figure 2. Photos of the powder mixture after 2(A), 4(B), 6(C), and 8(D) hours of mixing. SEM image of the powder mixture after 8 h of mixing (E).

calculated by dividing the length of the line by its number of intersections. The diameter of the grain would then be equal to the diameter of the circle that has the same area as the width × length.

The size distributions of the precipitates were measured using the ImageJ software. Multiple SEM images were taken and the size of the precipitates in the images was measured. The volume fraction, f_p , of the precipitates in the samples was measured using Equation I.

$$f_p = \frac{\frac{4}{3}\pi\left(\frac{d_p}{2}\right)^3 N_p}{Ad_p} \quad (I)$$

Where d_p is the mean diameter of the precipitates, N_p is the number of precipitates in a given area, and A is the area of the given area.

3. Results and discussion

3.1. Microstructures of as-printed samples

SEM images comparing the microstructures of as-printed samples are shown in [Figure 5A and B](#). The microstructures of both samples consist of a white color phase with a

Table 4. Labeling of IN718 and the composite samples

| Sample ID | Heat treatment | Reinforcement |
|-----------|-----------------------------|------------------------|
| AP-0 | As-printed | Nil |
| AP-Y | | Y_2O_3 |
| 1075-0 | Solutionized at 1075°C | Nil |
| 1075-Y | | Y_2O_3 |
| 1075A-0 | Solutionized at 1075°C+Aged | Nil |
| 1075A-Y | | Y_2O_3 |
| 1275A-0 | Solutionized at 1275°C+Aged | Nil |
| 1275A-Y | | Y_2O_3 |

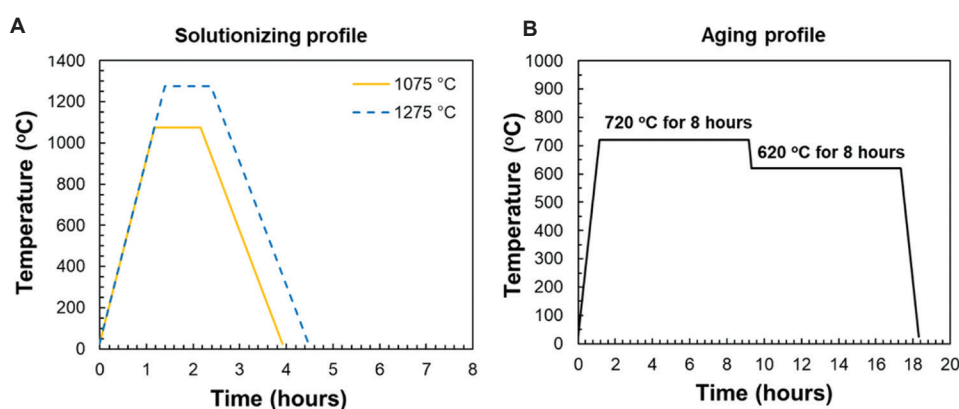


Figure 3. Solutionizing (A) and aging (B) profiles.

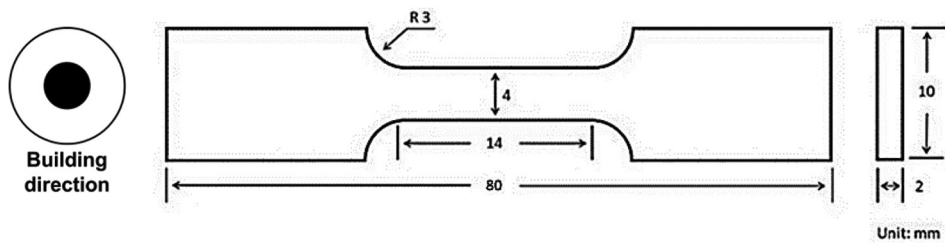


Figure 4. Dimensions of the tensile coupons used. The building direction is pointing out of the page.

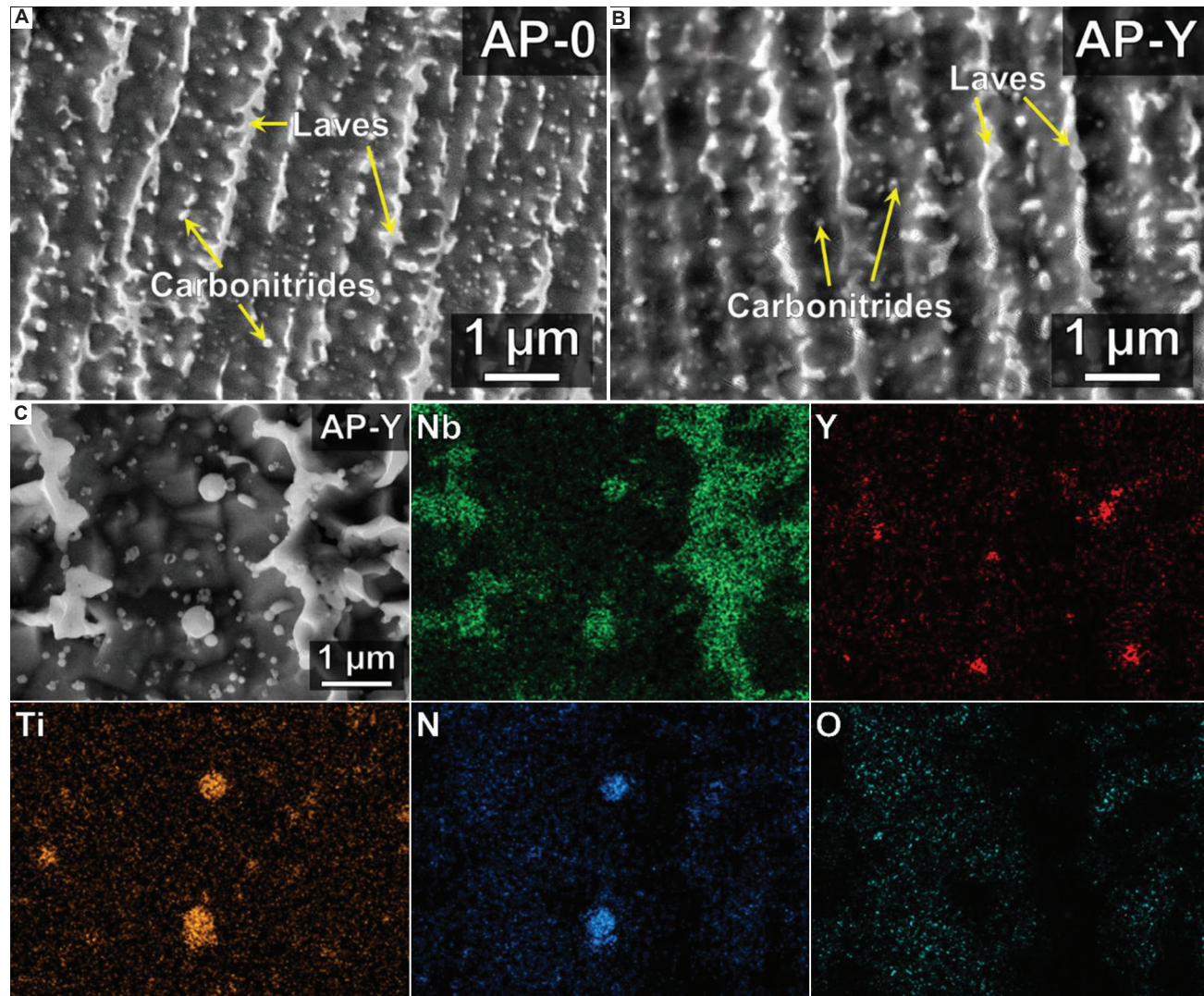


Figure 5. Scanning electron microscopy images of the microstructures of samples AP-0 (A) and AP-Y (B). EDX analysis of the phases in sample AP-Y (C).

long chain morphology and several nano-sized particles distributed throughout the microstructures. EDX analysis of sample AP-Y (Figure 5C) shows that the long chain phase consists of primarily Nb and Mo. On the other hand, the nano-sized particles are made up of primarily Ti, N, and Nb.

According to the phase transformation route during solidification of IN718, which is $L \Rightarrow L + \gamma \Rightarrow L + \gamma + \text{NbC} \Rightarrow L + \gamma + \text{NbC} + \text{Laves}$ ^[28], the Laves phase is the last phase to form when there is a high concentration of Nb and Mo in the liquid melt due to the low solubility limit of these elements in IN718^[29]. Due to the long chain phase

having high concentrations of Nb and Mo, it is identified to be Laves phase. This phase is usually located in the interdendritic region after solidification^[30]. Consequently, the nano-sized particles are identified to be NbC carbide precipitates. Even though element C is difficult to index, the identification of the phase is further supported by the presence of elements Ti and N in the precipitates. This is because the pre-existing TiN in the melt often acts as nucleation sites for the NbC precipitates due to favorable lattice match^[31]. Due to the presence of both C and N in the precipitates, they are also referred to as carbonitride precipitates. Moreover, Figure 5C shows that the Y_2O_3 nanoparticles are segregated at the interdendritic regions where the Laves phase is usually located.

The distributions of particle size in all as-printed samples are shown in Figure 6. It can be seen that the addition of the reinforcement particles increases the size of the precipitates in the IN718 matrix, which reflects the results shown in our previous study that Y_2O_3 nanoparticles have a high tendency to combine with the existing carbonitride precipitates and increase in size^[23]. The majority of the precipitates in sample AP-0 are in the range of 45 – 65 nm in diameter while it is 55 – 95 nm in diameter in sample AP-Y as shown in Figure 6A. Furthermore, the cumulative percentage graph of sample AP-0 is always above that of sample AP-Y as shown in Figure 6B. This shows that at any particular particle diameter size, there is a higher proportion of precipitates in sample AP-0 that are smaller than and equal to that diameter size. The specific d_{10} , d_{50} , d_{90} , and the mean particle diameter, d_p , values of the size of the precipitates are listed in Table 5.

Table 5. Comparison of d_{10} , d_{50} , d_{90} , and d_p values of the size of the precipitates in the as-printed samples

| Sample ID | d_{10} (nm) | d_{50} (nm) | D_{90} (nm) | d_p (nm) |
|-----------|---------------|---------------|---------------|------------|
| AP-0 | 37.2 | 51.5 | 84.7 | 62.5 |
| AP-Y | 50.6 | 72.3 | 114.9 | 83.7 |

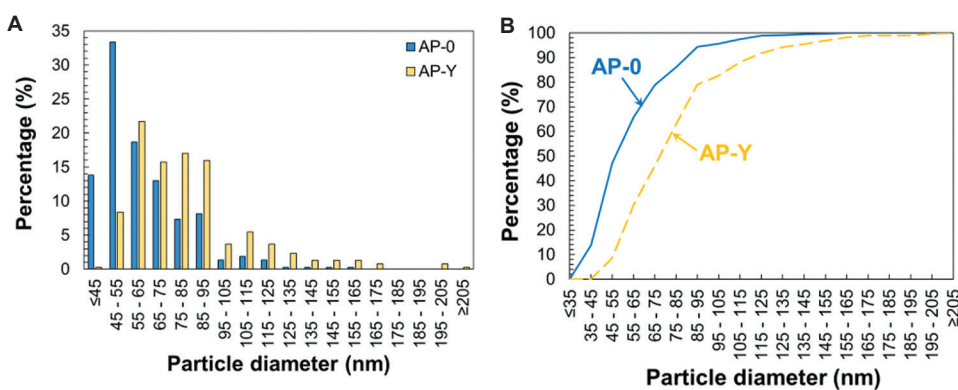


Figure 6. The size distribution (A) and the cumulative percentage (B) of the precipitates in the as-printed samples.

3.2. Microstructures of printed samples after 1075°C solutionized and aged

Both monolithic and Y_2O_3 -reinforced samples solutionized at 1075°C are deeply etched to reveal their microstructures as shown in Figure 7. It can be seen that the grain structures of both samples consist of mostly columnar grains with some equiaxed grains distributed throughout, both after solutionizing and after aging treatments. The optical micrographs also reveal that the grains' interior (in between the black dashed lines that indicate the grain boundaries) of the samples after aging (Figure 7B and D) is darker than that of the samples before aging (Figure 7A and C).

SEM analysis in Figure 8 shows that the grains' interior consists of numerous precipitates either arranged in straight lines or randomly distributed. Since a higher number of these precipitates are observed in both samples after aging, the darker grains' interior observed in Figure 7 corresponds to this increase in precipitate formation. SEM analysis reveals that the Laves phase at the grain boundaries (as indicated in Figure 8) has a discrete and blocky morphology. This phenomenon is observed in both the monolithic IN718 sample (Figure 8A) and the composite (Figure 8C). However, the morphology of the Laves phase does not change significantly after aging as shown in (Figure 8B and D). It should be noted that the grain boundaries Laves phase in both samples 1075-0 and 1075A-0 appears to be larger and more concentrated compared to samples 1075-Y and 1075A-Y.

A closer look using SEM shows that the interdendritic Laves phase transforms from a straight, long-chain, and continuous morphology (Figure 5A and B) to also a discrete and blocky morphology after solutionizing treatment, similar to the one located at grain boundaries but smaller in size. The microstructures of both samples 1075-0 and 1075-Y (Figure 9) consist of mostly Laves phase and δ phase. The presence of the δ phase after solutionizing treatment is due to the following reasons. First, as Laves

phase dissolves during the heat treatment, the amount of Nb available in the matrix increases. This provides extra material for the formation of δ phase, which has a chemical formula of Ni_3Nb . Second, according to the TTT diagram of IN718, the δ phase starts to form at approximately 980°C, which is below the solutionizing temperature.

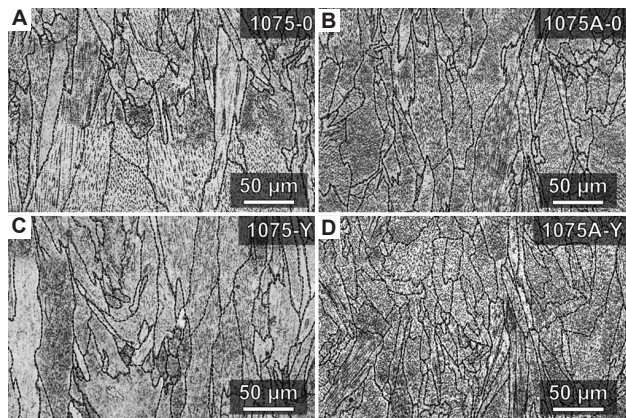


Figure 7. Optical micrographs of etched samples 1075-0 (A), 1075A-0 (B), 1075-Y (C), and 1075A-Y (D). The black dashed lines indicate the grain boundaries.

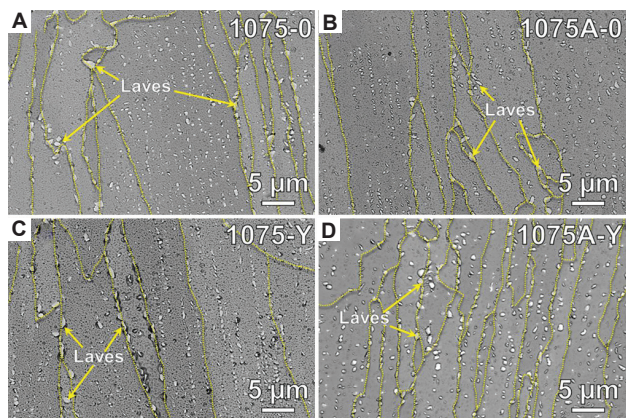


Figure 8. Scanning electron microscopy images showing the microstructures of samples 1075-0 (A), 1075A-0 (B), 1075-Y (C), and 1075A-Y (D). The yellow dashed lines indicate the grain boundaries.

Due to the sample being furnace-cooled at the end of the solutionizing treatment, this provides extra time for the δ phase to form.

Further analysis of sample 1075-Y shows that multiple nano-sized precipitates can be observed near or embedded inside the Laves phase particles as shown in [Figure 10A](#). Extensive analysis by line scan EDX shows that the compositions of the precipitates are a combination of Nb, Ti, Y, N, and O elements. The precipitates that are embedded in the Laves phase particles have 1 common trait, which is the presence of Ti and N in all of them, as shown in Region 2 in [Figure 10B](#) and Region 1 in [Figure 10D](#). On the other hand, Y may or may not be detected in those precipitates as shown in the presence of Y peak in Region 1 in [Figure 10D](#) but not in Region 2 in [Figure 10B](#). However, it can also be seen that O can be detected in both cases of embedded precipitates, suggesting that Y could also be present but only in a minute amount. Most of the time, the precipitates that exist outside of the Laves phase have both Y and Ti as well as O, while N is not detected. This can be observed in Region 1 in [Figure 10B](#) and Region 2 in [Figure 10D](#). Due to the lack of element N, these precipitates that are observed in sample 1075-Y are the Y-Ti-O complex precipitates that were reported in other literature^[32,33].

However, the precipitate formation that is similar to the observed precipitates in sample AP-Y can still be found in sample 1075-Y as shown in Region 3 in [Figure 10D](#). In addition, large Y_2O_3 particles and large TiN particles can be detected next to each other as shown in Regions 1 and 2 in [Figure 10C](#). As such, all these observations further support the conclusion made previously in which Y_2O_3 nanoparticles have a high tendency to combine with other elements in the IN718 to form complex precipitates.

After the IN718/ Y_2O_3 composite has been solutionized, two additional observations can be made. First, the presence of embedded precipitates within the Laves phase suggests that reprecipitation of Laves phase during cooling has occurred and trapped other precipitates within

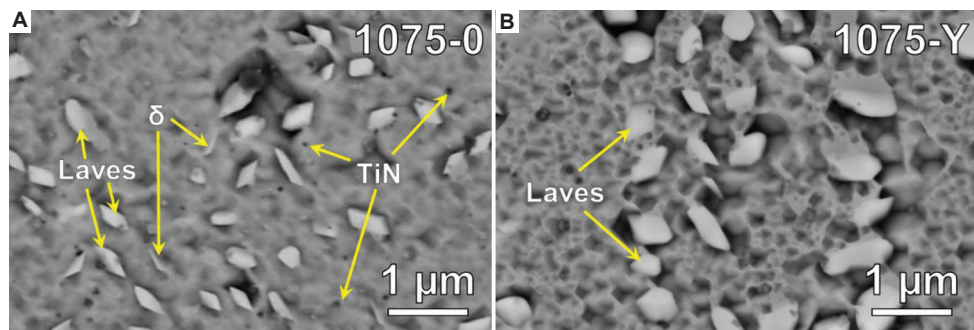


Figure 9. Scanning electron microscopy images showing the microstructures of samples 1075-0 (A) and 1075-Y (B).

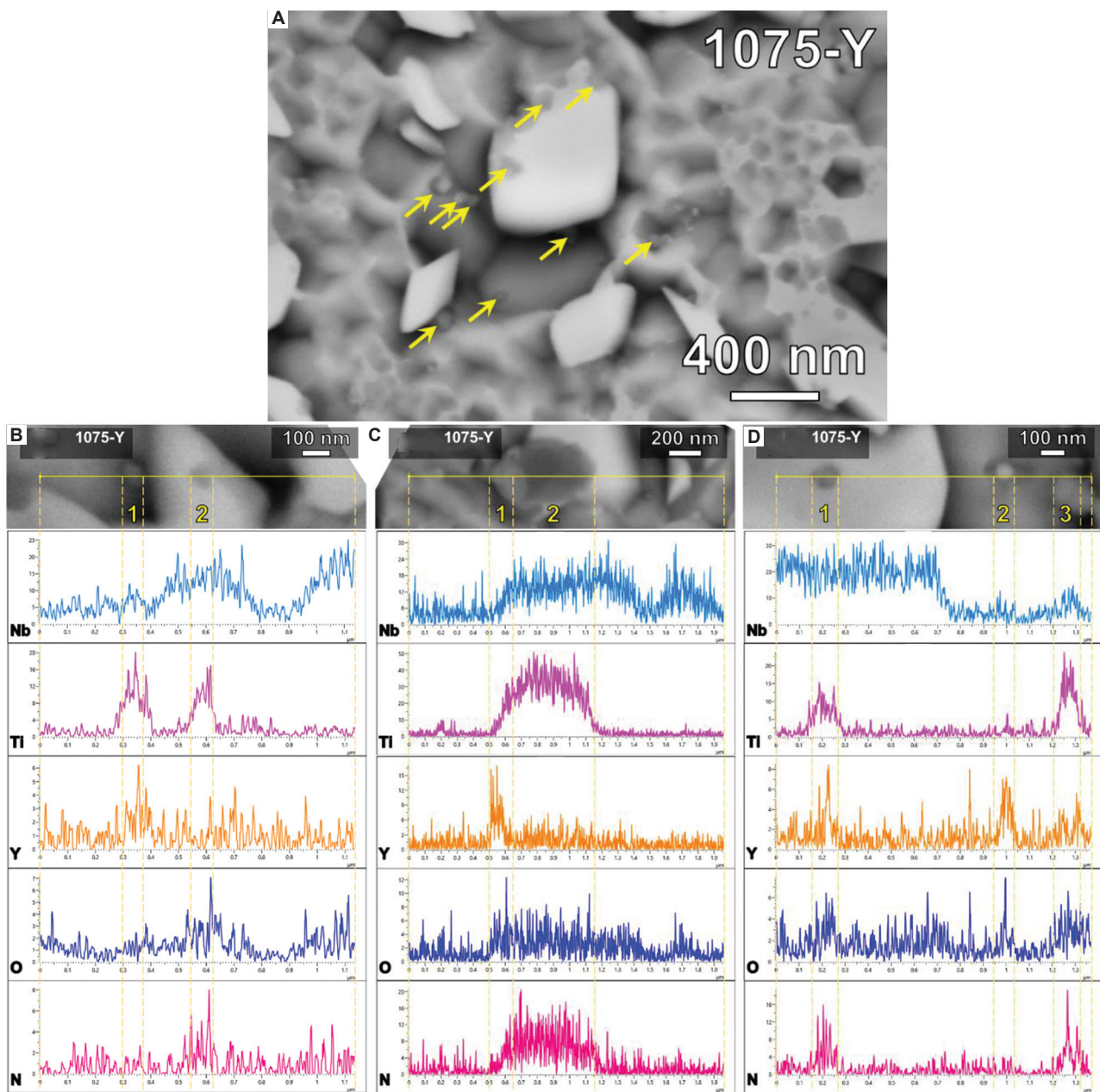


Figure 10. Scanning electron microscopy image showing precipitates (yellow arrows) present in the microstructure of sample 1075-Y (A). Line scan EDX (B–D) analysis showing the variation of chemical compositions (wt.%) across different precipitates in sample 1075-Y.

them. As Y_2O_3 has a high tendency to combine with Ti, these elements are often found together in the Laves phase. Second, the appearance of numerous nano-sized Y-Ti-O precipitates with diameters <100 nm suggests that those precipitates were formed during the solutionizing treatment. Shi *et al.*^[34] observed a similar phenomenon in heat-treated Zr-containing ODS-FeCrAl in which nano-sized Y-Al-O precipitates were formed during solutionizing treatment. The authors attributed this to the supersaturated

state of Y in the matrix in the as-printed sample. When the as-printed sample is subjected to solutionizing treatment, the element Y is released, forming the observed nano-sized precipitates. Moreover, the absence of N in the complex precipitates when they are not embedded inside the Laves phase particle prevents the NbC shell from forming properly due to the lack of a favorable TiN nucleation site. Thus, the size of the complex precipitate is significantly smaller.

The grain sizes of the printed samples after different stages of heat treatment are listed in **Table 6**. It can be seen that the grain size of the as-printed IN718/ Y_2O_3 composite sample is slightly larger than that of the as-printed monolithic IN718 sample. The limited grain refinement effect in the as-printed IN718/ Y_2O_3 composite sample is the result of the low wettability between the Y_2O_3 nanoparticles and the IN718 matrix, which makes them not effective as nucleation sites^[35]. However, after solutionizing and aging, there is an increase in equiaxed grains formation in the Y_2O_3 -reinforced sample after heat treatment as shown in **Figure 7C and D**. Due to this, the average grain size of the Y_2O_3 -reinforced sample decreases from 19.1 ± 3.1 (before heat treatment) to $17.1 \pm 7.2 \mu\text{m}$ (after solutionizing) to $12.5 \pm 4.1 \mu\text{m}$ (after aging).

Table 6. Grain sizes (μm) of the printed samples at different stages of heat treatment

| Reinforcement | As-printed | 1075°C solutionized | 1075°C solutionized+aged |
|-------------------------------|----------------|---------------------|--------------------------|
| Nil | 18.9 ± 1.9 | 23.8 ± 8.2 | 18.9 ± 4.4 |
| 1 wt.% Y_2O_3 | 19.1 ± 3.1 | 17.1 ± 7.2 | 12.5 ± 4.1 |

$\pm 4.1 \mu\text{m}$ (after aging). On the other hand, the grain size of the monolithic sample increases from $18.9 \pm 1.9 \mu\text{m}$ to $23.8 \pm 8.2 \mu\text{m}$ after solutionizing and decreases to $18.9 \pm 4.4 \mu\text{m}$ after aging. It should be noted that both samples achieve grain refinement after aging but the effect is stronger in the Y_2O_3 -reinforced sample as the grain size decreases by 26.9% compared to 20.6% in the monolithic sample. This suggests that both the existing carbonitride precipitates and the newly formed nano-sized Y-Ti-O precipitates contribute to the grain refinement. These precipitates aid the grain recrystallization at high temperature by acting as nucleation centers. As such, due to the absence of the Y-Ti-O precipitates in the monolithic samples, the carbonitride precipitates alone are not enough to suppress grain growth due to the high temperature^[36] during solutionizing treatment. This results in a bigger grain size in the solutionized monolithic sample.

3.3. Mechanical properties of heat-treated IN718 composites

A comparison of the mechanical properties between monolithic samples and Y_2O_3 -reinforced samples is shown in **Figure 11A**. All samples were fabricated using their

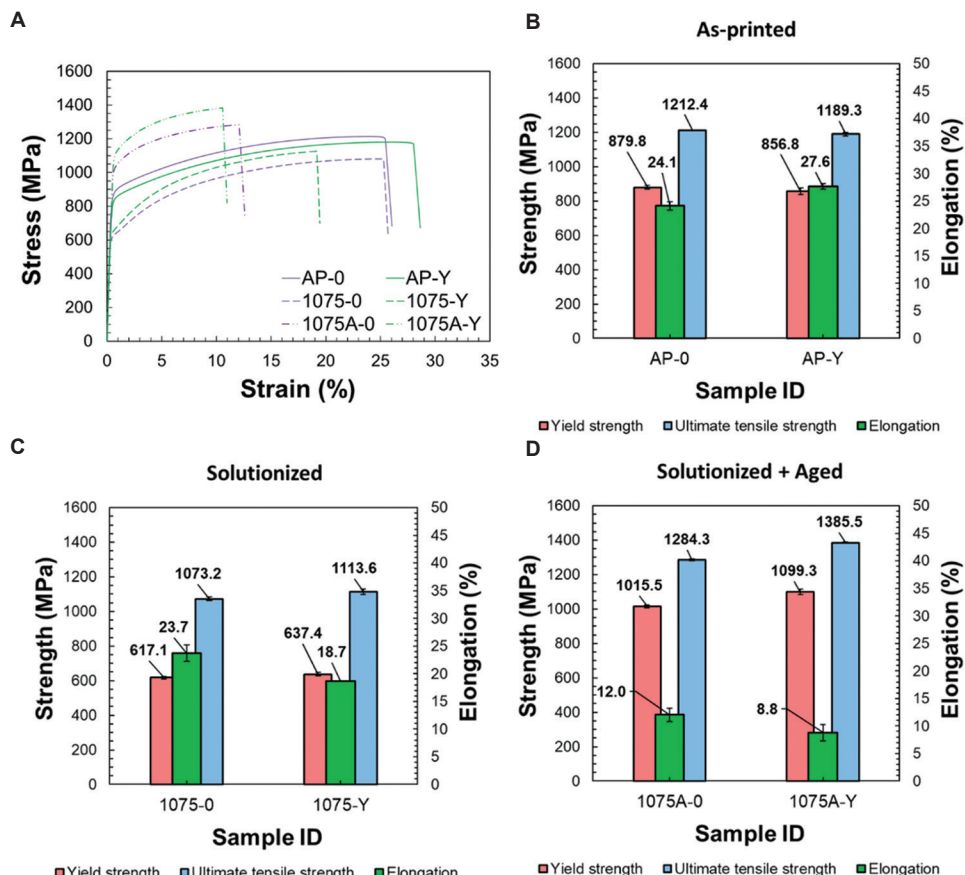


Figure 11. Stress-strain curves comparing monolithic samples with Y_2O_3 -reinforced samples (A). Tensile properties of as-printed (B), after solutionized (C), and after solutionized + aged (D) Y_2O_3 -reinforced samples in comparison with monolithic samples.

optimized parameters and solutionized at 1075°C so that the best mechanical properties could be obtained. This is because at this temperature, the Laves phase is dissolved almost completely and the remaining Laves phase has a particulate morphology instead of a long chain morphology. Furthermore, the amount of δ phase precipitates in the microstructure is kept relatively low as this phase also has several negative impacts on the mechanical properties^[37]. The strength and elongation values after each heat treatment stage are shown in Figure 11B to D.

It can be seen that sample AP-Y has higher elongation than that of sample AP-0 (27.6% compared to 24.1%) while the strength of sample AP-Y (yield strength [YS] and ultimate tensile strength [UTS] are 856.8 and 1189.3 MPa, respectively) is slightly lower than that of sample AP-0 (YS and UTS are 879.8 and 1212.4 MPa, respectively). After being solutionized, a significant decrease in strength is observed in the monolithic sample in which YS and UTS both decrease by 29.9% and 11.5%, respectively. However, the extent of the reductions in YS and UTS in the Y_2O_3 -reinforced sample is lesser, which are 25.6% and 6.4%, respectively. After both solutionizing and aging treatments are done, the strength of the Y_2O_3 -reinforced sample (YS and UTS are 1099.3 and 1385.5 MPa, respectively) continues to be higher than that of the monolithic sample (YS and UTS are 1015.5 and 1284.3 MPa, respectively).

By considering the contribution of different strengthening factors, the minor differences in the strength of the as-printed samples can be explained as follows. First, as nanoscale carbonitride precipitates are also present in the base material, it is reasonable to also include their Orowan strengthening contribution. The contribution of Orowan strengthening, σ_{Orowan} , is calculated using Equation II^[38].

$$\sigma_{\text{Orowan}} = \frac{0.538Gb\sqrt{f_p}}{d_p} \ln\left(\frac{d_p}{2b}\right) \quad (\text{II})$$

Where G is the shear modulus and b is the Burgers vector. For IN718, $G = 63 \text{ Gpa}$ ^[39] and $b = \frac{a}{2}110$ ^[40], where a is the lattice parameter of IN718, which $a = 0.359 \text{ nm}$ ^[41]. Thus, $b = 0.2539 \text{ nm}$.

However, the increase in strength due to Orowan strengthening in sample AP-Y is calculated to be only 12.34 MPa higher than that of sample AP-0. As such, due to the presence of the carbonitride precipitates in sample AP-0, the contribution of Orowan strengthening in sample AP-Y is only significant if it is noticeably higher than the contribution of the carbonitride precipitates. However, it can be seen that the addition of reinforcement particles

increases the size of the carbonitride precipitates. Thus, the increase in Orowan strengthening is small.

Second, the strength of the as-printed samples is also affected by the grain size through grain boundary strengthening or the Hall-Petch strengthening effect. However, due to the small difference in the grain size of samples AP-0 and AP-Y as shown in Table 6, the difference in the Hall-Petch strengthening effect is also negligible.

In addition to the stated strengthening mechanisms, other mechanisms such as the coefficient of thermal expansion (CTE) mismatch strengthening mechanism or the load transfer mechanism can also strengthen the material. The CTE mismatch strengthening, $\Delta\sigma_{\text{CTE}}$, can be calculated using Equation III^[42].

$$\Delta\sigma_{\text{CTE}} = kGb \sqrt{\frac{12'' T(\alpha_m - \alpha_p)f_p}{bd_p(1-f_p)}} \quad (\text{III})$$

Where k is a constant approximately equal to 1.25, ΔT is the difference between the processing and testing temperatures, α_m and α_p are the coefficient of thermal expansion of matrix and reinforcement particles, respectively. The theoretical volume fraction of the nanoparticles will be used for calculation. The processing temperature for LPBF can be taken to be 2100 K^[43], thus $\Delta T = 2100 - 300 = 1800 \text{ K}$. Using the theoretical vol% of the added nano-

Y_2O_3 particles, $d_{p(\text{Y}_2\text{O}_3)} = 65 \text{ nm}$, $\alpha_m = 13.1 \times 10^{-6} \text{ K}^{-1}$ ^[44], and $\alpha_{p(\text{Y}_2\text{O}_3)} = 8.1 \times 10^{-6} \text{ K}^{-1}$ ^[45], the contribution of $\Delta\sigma_{\text{CTE}}$ in sample AP-Y is calculated to be 207.85 MPa.

Thus, based on the calculated results, CTE mismatch is indeed one of the important strengthening mechanisms in the IN718/ Y_2O_3 composite due to the significant increase in the sample strength. This is also verified by Wang *et al.*^[42] in which the calculated contribution of CTE mismatch strengthening is the highest. However, it has been reported that the inclusion of CTE mismatch strengthening often overestimates the actual strength of the sample. As such, several papers agreed that the activation of CTE mismatch strengthening is questionable and thus could be negligible^[46-50]. Furthermore, it has also been shown that CTE mismatch strengthening can only be significant when the reinforcement particles are above a certain size^[51] and volume fraction^[52]. The critical diameter, d_c can be calculated using Equation IV.

$$d_c = \frac{b}{\Delta\alpha\Delta T} \quad (\text{IV})$$

In this case, the d_c of the nano- Y_2O_3 particles is calculated to be 91.4 nm. As the mean diameter of the Y_2O_3 nanoparticles is 65 nm, the majority of them are

below the critical diameter. In addition, due to the small volume fraction of the added nanoparticles, the fraction of the nanoparticles that can contribute to strengthening is also small.

Furthermore, the previously calculated results of the strengthening contribution are based on the CTE mismatch between the Y_2O_3 nanoparticles and the IN718 matrix. However, it has been pointed out that the nanoparticles have a high tendency to combine with the carbonitride shell to form a complex precipitate. As such, it would be more appropriate to compare the CTE mismatch between the Y_2O_3 nanoparticles and the carbonitride shell. Since the CTE of the shell is in the range of $6.65 \times 10^{-6}\text{K}^{-1}$ to $8.48 \times 10^{-6}\text{K}^{-1}$ ^[53], which is much closer to that of the Y_2O_3 nanoparticles than IN718 is, the actual increase in strength is again expected to be small. Due to these reasons, the contribution of CTE mismatch strengthening in the IN718/ Y_2O_3 composite will be omitted.

Finally, the load transfer mechanism, $\Delta\sigma_{load}$ can be calculated using Equation V^[42,54].

$$\Delta\sigma_{load} = 0.5f_p\sigma_m \quad (\text{V})$$

Where σ_m is the yield strength of the matrix. It can be seen from Equation V that the contribution of the load transfer mechanism is expected to be small as the volume fraction, f_p , of the reinforcement particles is very small. Coupling with the 0.5 coefficient, the load transferring mechanism is believed to be not at play, which is also verified by Wang *et al.*^[42]

Thus, it can be seen that the majority of the strengthening mechanisms do not result in a significant improvement in the strength of sample AP-Y. In fact, the strength of sample AP-Y is slightly lower than that of sample AP-0. This is because the theoretical calculation does not consider the agglomeration of the Y_2O_3 nanoparticles. This further supports the observations made in Section 3.1 in which there is a high concentration of Y_2O_3 in the interdendritic regions. As a result, this overestimated the strengthening contribution of the Orowan mechanism. Furthermore, several other factors could potentially overestimate the Orowan strengthening mechanism such as not all the particles being spherical and the mean particle diameter values being inaccurate to represent the entire size distribution. Thus, due to the similar grain sizes, the small volume fraction of reinforcement particles, and the presence of carbonitride precipitates in sample AP-0, the strengths of the as-printed samples only differ slightly.

However, in this study, the value added of the reinforcement particles in strengthening IN718 can only be realized after heat treatment as seen in

Figure 11. A thorough quantitative analysis of the Orowan strengthening is challenging in heat-treated samples since there are numerous types of nano-sized precipitates (carbonitride precipitates, Y_2O_3 nanoparticles, Y-Ti-O nanoparticles, γ' and γ'' precipitates, and δ and blocky Laves phase) that each contributes to the strength of the material differently. Furthermore, the morphology of the majority of the precipitates is not spherical and their distribution in the matrix may not be homogeneous. Thus, these factors make quantifying the contribution of the precipitates to the strength of the material highly challenging. However, an appropriate qualitative analysis to explain the differences in the material's strength can still be carried out.

First, the number of nano-sized precipitates in the Y_2O_3 -reinforced sample is expected to be higher than in the monolithic sample due to the formation of the Y-Ti-O precipitates after solutionizing treatment (Figure 10A). As such, these precipitates increase the strength of the IN718/ Y_2O_3 composite after heat treatment. Furthermore, these precipitates also contribute to grain refinement after heat treatment since they act as nucleation centers for the recrystallization of grains at high temperatures and at the same time, suppress grain growth. Hence, this further enhances the material's strength through grain boundary strengthening.

Second, it is theorized that the difference in the Laves phase morphology at the grain boundaries between the Y_2O_3 -reinforced samples and the monolithic samples as shown in Figure 8 also contributes to the difference in the mechanical properties. However, after solutionizing treatment at 1075°C, the microstructural changes resulting from additional aging treatment are not obvious. Thus, it is challenging to accurately characterize the differences. As such, to accurately characterize the differences in the microstructures that arise from aging treatment and to understand the reasons behind any changes in mechanical properties after aging treatment, both samples are solutionized at 1275°C before aging. This is because when the samples are solutionized at this temperature, the diffusion of different alloying elements is significantly enhanced^[55]. As such, the movements of the alloying elements during heat treatment can be visualized.

SEM analysis of sample 1275A-Y shows that the addition of Y_2O_3 has resulted in grain refinement. This is evident in Figure 12 showing a significantly higher number of smaller equiaxed grains in sample 1275A-Y compared to sample 1275A-O. It is also observed that the segregated regions (red color) are thinner in sample 1275A-Y than those in sample 1275A-O. This further reinforced the phenomenon in which the addition of Y_2O_3 reduces the segregation at the grain boundaries as shown in Figure 8.

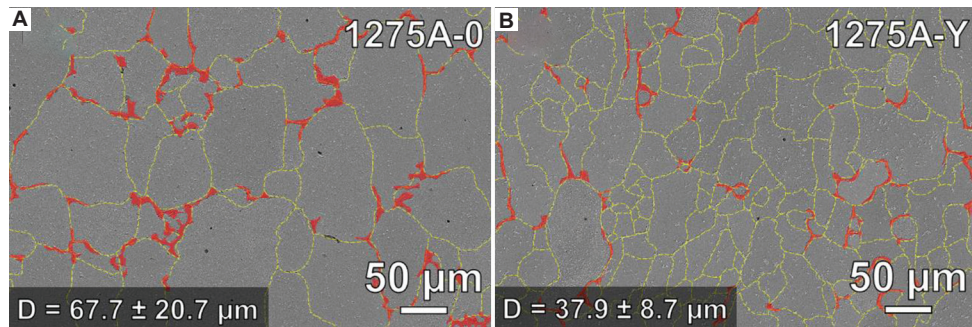


Figure 12. SEM images of samples 1275A-0 (A) and 1275A-Y (B) showing the grain boundaries (yellow dashed lines) and segregated regions (red areas). D: grain size.

In-depth analysis of the grain boundary of sample 1275A-Y (Figure 13) revealed that the segregated region consists of numerous small precipitates embedded within the segregated material as shown in Figure 13B. On the other hand, the non-segregated region consists of a cluster of several white color precipitates as shown in Figure 13C.

EDX analysis shows that in segregated regions, the embedded is either Y_2O_3 or TiN particles. In addition, Nb is not detected in any of the particles. A similar observation can be made in the non-segregated region in which individual Y_2O_3 and TiN particles cluster together. Combined with the information in Figure 10, this shows that the complex precipitates that exist in the as-printed sample are not stable at high temperatures for a prolonged period and gradually separate into individual Y_2O_3 and TiN particles.

The increase in the number of precipitates increases the effectiveness of the Zener pinning effect, suppressing grain growth^[56]. As such, significant grain refinement is observed in sample 1275A-Y as the grain size decreases from $67.7 \pm 20.7 \mu\text{m}$ to $37.9 \pm 8.7 \mu\text{m}$ as shown in Figure 12. The grain refinement in sample 1075A-Y suggests that the same phenomenon could have occurred in that sample. As there are more grain boundaries in sample 1275A-Y than in sample 1275A-0, there are more sites for the material to diffuse toward, resulting in thinner segregated regions as shown in Figure 12B.

It is also observed that the distribution of the γ' and γ'' precipitates in sample 1275A-Y have less of a difference as compared to those in sample 1275A-0 as shown in Figure 14. It is generally accepted that the γ' phase has a cube-shaped morphology^[57] while the γ'' phase has a disc-shaped morphology^[58]. The precipitates are indicated in Figure 14A and C. The γ' and γ'' precipitates are seen abundantly near the grain boundaries in sample 1275A-0 (Figure 14A). It is calculated that the precipitates occupied 71.0% of the total area of the

image. However, in the region that is far from the grain boundaries, few precipitates are seen (Figure 14B), which only occupied 52.0%. On the other hand, the difference in the occupied area of the precipitates between near and far from the grain boundaries in sample 1275A-Y is only 2.4%, which is significantly smaller than the 19.0% in sample 1275A-0.

The reason for the differences is as follows. It has been established that the segregation of Nb at the grain boundaries is much more severe in sample 1275A-0. In addition, the grain size of sample 1275A-0 is also much larger than that of sample 1275A-Y. Figure 15 shows the schematics that visualize the difference in the distribution of Nb in the microstructures between samples 1275A-0 and 1275A-Y. Due to the larger grain size and the segregation of Nb at the grain boundaries in sample 1275A-0, there is an Nb concentration gradient from the center of the grain to the edge of the grain as Nb diffuses towards the grain boundaries. Thus, this creates regions of low concentration of Nb at the center of the grains (red color) and regions of high concentration of Nb near the segregated materials at the grain boundaries (blue color). On the other hand, due to the smaller grain size of sample 1275A-Y, while having much less segregation at the grain boundaries, the concentration gradient of Nb in the microstructure is also much less significant. Thus, the distribution of Nb in sample 1275A-Y is relatively homogeneous. As Nb is needed for the formation of both the γ' and γ'' precipitates, there will be more and bigger precipitates in the blue regions in sample 1275A-0 due to the abundance of Nb. On the other hand, there is not enough Nb in the red region for the precipitates to form properly. Thus, this explains the difference observed in Figure 14A and B. Due to the relatively homogeneous distribution of Nb in sample 1275A-Y, the difference observed in Figure 14C and D is not significant. Because sample 1075A-Y also has a smaller grain size and less segregation at the grain boundaries compared to sample

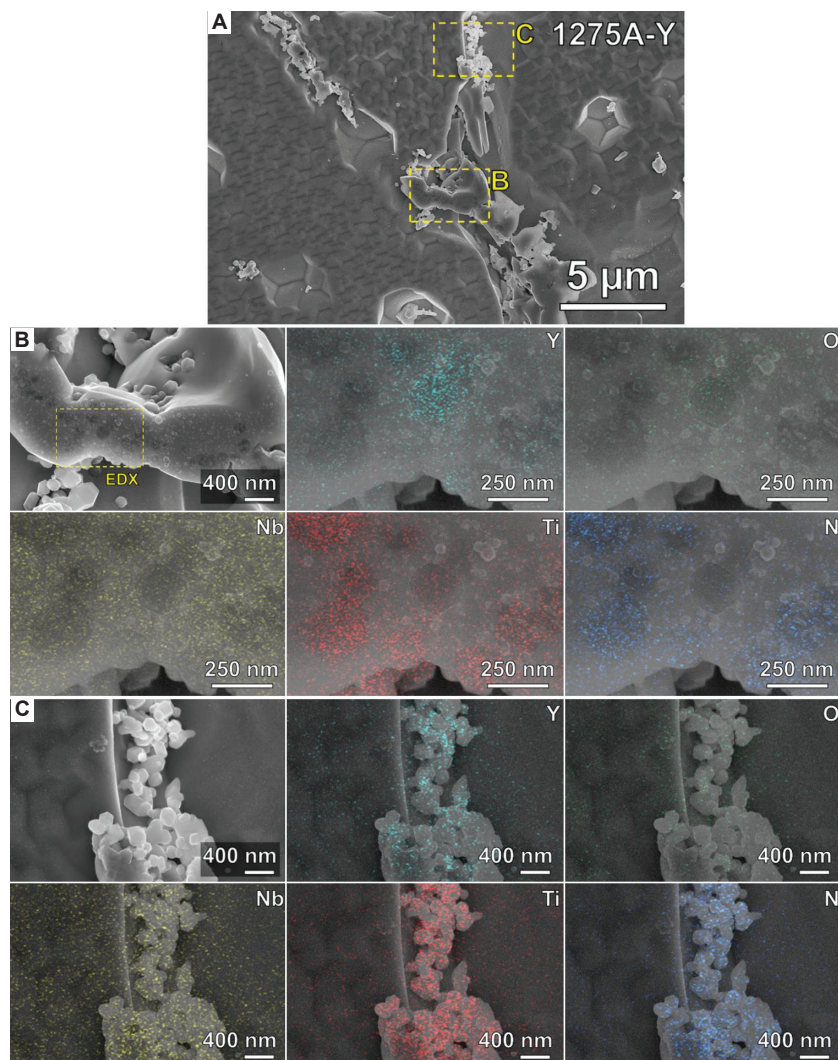


Figure 13. Scanning electron microscopy (SEM) images showing the grain boundary of sample 1275A-Y (A). High-magnification SEM images with EDX mapping spectra of the segregated (B) and non-segregated (C) areas.

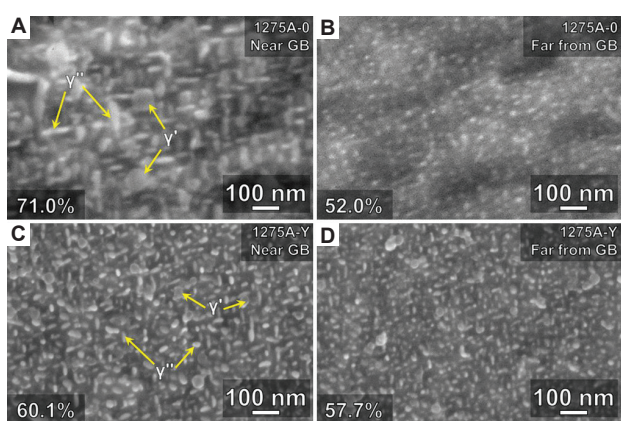


Figure 14. Scanning electron microscopy images showing the precipitates in sample 1275A-0 near grain boundary (A) and far from grain boundary (B), and in sample 1275A-Y near grain boundary (C) and far from grain boundary (D). GB: grain boundary.

1075A-0, the distribution of the γ' and γ'' precipitates is expected to follow the same trend.

Thus, while it is true that the presence of γ' and γ'' precipitates after aging treatment increases the strength of both Y_2O_3 -reinforced and monolithic samples significantly, the distribution of the precipitates is shown to be affected by the addition of the reinforcement particles, which, in turn, affects their effectiveness. The lack of proper precipitation in the region far away from the grain boundaries in sample 1275A-0 affects the mechanical properties of the heat-treated monolithic sample negatively. Taken together, the higher strengths of the composites are the result of the increased Orowan strengthening from a significantly higher number of nano-sized precipitates, the grain boundary strengthening effect, and the γ' and γ'' precipitates being distributed more homogeneously.

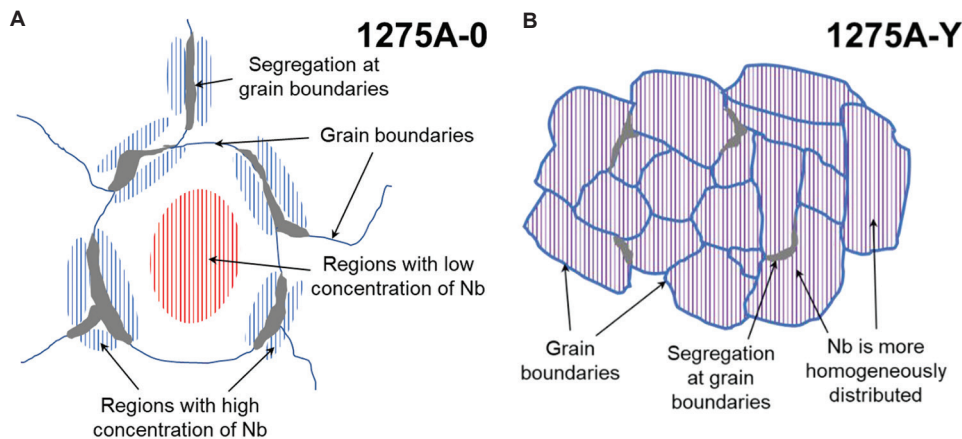


Figure 15. Schematics showing the difference in the distribution of Nb in the microstructures between samples 1275A-0 (A) and 1275A-Y (B).

4. Conclusions

The influence of Y_2O_3 addition on the microstructures of heat-treated LPBF IN718 samples is investigated, and the results are as follows.

- Y_2O_3 nanoparticles have a high tendency to combine with carbonitride precipitates to form complex precipitates. These complex precipitates separate into individual Y_2O_3 and TiN nanoparticles after heat treatment. At the same time, Y-Ti-O precipitates form during the heat treatment due to the release of supersaturated Y in the matrix.
- Grain refinement is observed in the Y_2O_3 -reinforced composite after heat treatment due to the high number of nano-sized precipitates acting as nucleation centers for the recrystallization of grains and suppressing grain growth as a result of the Zener pinning effect.
- Thinner segregated regions are observed at the grain boundaries of the heat-treated Y_2O_3 -reinforced composite. This leads to a more homogeneous distribution of Nb in the microstructures and results in a smaller difference in the γ' and γ'' precipitates distribution between the regions near and far from the grain boundaries.
- The value added of the reinforcement particles in strengthening IN718 is only realized after heat treatment. The higher strengths of the composites are the result of the increased Orowan strengthening from a significantly higher number of nano-sized precipitates, the grain boundary strengthening effect, and the γ' and γ'' precipitates being distributed more homogeneously.

Acknowledgments

The work is supported by the A*STAR Graduate Academy (A*GA) and by the Nanyang Technological University

(NTU). The authors would like to thank Mr. Min Hao Goh for his assistance with the SEM-EDX analysis and Dr. Li Tao for his assistance with the heat treatment.

Funding

The financial support from the A*STAR Structural and Metal Alloys Program (SMAP): Work Package II with project No. A18B1b0061 is acknowledged.

Conflict of interest

The authors declare that they have no known competing financial interests or personal relationships that could have appeared to influence the work reported in this paper.

Author contributions

Conceptualization: Duy Nghia Luu and Wei Zhou

Formal analysis: Duy Nghia Luu

Investigation: Duy Nghia Luu

Methodology: Duy Nghia Luu

Project administration: Wei Zhou and Sharon Mui Ling Nai

Resources: Wei Zhou and Sharon Mui Ling Nai

Supervision: Wei Zhou and Sharon Mui Ling Nai

Validation: Wei Zhou and Sharon Mui Ling Nai

Visualization: Duy Nghia Luu

Writing – original draft: Duy Nghia Luu

Writing – review and editing: Wei Zhou and Sharon Mui Ling Nai

References

- Ibrahim IA, Mohamed FA, Lavernia EJ, 1991, Particulate reinforced metal matrix composites-a review. *J Mater Sci*, 26: 1137–1156.
<https://doi.org/10.1007/BF00544448>
- Gu DD, Meiners W, Wissenbach K, et al., 2012, Laser additive manufacturing of metallic components: Materials,

- processes and mechanisms. *Int Mater Rev*, 57: 133–164.
<https://doi.org/10.1179/1743280411Y.0000000014>
3. Zhang YC, Li ZG, Nie PL, et al., 2013, Effect of ultrarapid cooling on microstructure of laser cladding IN718 coating. *Surf Eng*, 29: 414–418.
<https://doi.org/10.1179/1743294413Y.0000000142>
 4. Singh L, Singh B, Saxena KK, 2020, Manufacturing techniques for metal matrix composites (MMC): An overview. *Adv Mater Process Technol*, 6: 224–240.
<https://doi.org/10.1080/2374068X.2020.1729603>
 5. Sharma V, Prakash U, Kumar BV, 2015, Surface composites by friction stir processing: A review. *J Mater Process Technol*, 224: 117–134.
<https://doi.org/10.1016/j.jmatprotec.2015.04.019>
 6. Akbari M, Asadi P, Asiabaraki HR, 2022, Investigation of wear and microstructural properties of A356/TiC composites fabricated by FSP. *Surf Rev Lett*, 29: 1–10.
<https://doi.org/10.1142/S0218625X2250130X>
 7. Akbari M, Asadi P, 2021, Simulation and experimental investigation of multi-walled carbon nanotubes/aluminum composite fabrication using friction stir processing. *Proc Inst Mech Eng Part E J Process Mech Eng*, 235: 2165–2179.
<https://doi.org/10.1177/09544089211034029>
 8. Rohatgi PK, Asthana R, Das S, 1986, Solidification, structures, and properties of cast metal-ceramic particle composites. *Int Met Rev*, 31: 115–139.
<https://doi.org/10.1179/imtr.1986.31.1.115>
 9. Shi Z, Han F, 2015, Microstructures and properties of cast T91-ODS alloys. *Mater Res Innov*, 19: S5832–S5835.
<https://doi.org/10.1179/1432891714Z.0000000001202>
 10. Etemadi R, Wang B, Pillai KM, et al., 2018, Pressure infiltration processes to synthesize metal matrix composites-A review of metal matrix composites, the technology and process simulation. *Mater Manuf Process*, 33: 1261–1290.
<https://doi.org/10.1080/10426914.2017.1328122>
 11. S-De-la-muela AM, Cambronero LE, Ruiz-Román JM, 2020, Molten metal infiltration methods to process metal matrix syntactic foams. *Metals (Basel)*, 10: 149.
<https://doi.org/10.3390/met10010149>
 12. Kong D, Dong C, Ni X, et al., 2019, Effect of TiC content on the mechanical and corrosion properties of Inconel 718 alloy fabricated by a high-throughput dual-feed laser metal deposition system. *J Alloys Compd*, 803: 637–648.
<https://doi.org/10.1016/j.jallcom.2019.06.317>
 13. Gu D, Zhang H, Dai D, et al., 2019, Laser additive manufacturing of nano-TiC reinforced Ni-based nanocomposites with tailored microstructure and performance. *Compos Part B Eng*, 163: 585–597.
<https://doi.org/10.1016/j.compositesb.2018.12.146>
 14. Tang B, Tan Y, Zhang Z, et al., 2020, Effects of process parameters on geometrical characteristics, microstructure and tribological properties of TiB_2 reinforced Inconel 718 alloy composite coatings by laser cladding. *Coatings*, 10: 76.
<https://doi.org/10.3390/coatings10010076>
 15. Dhanya MS, Shukla AK, Dineshraj S, et al., 2019, Processing and characterization of yttria-dispersed Inconel 718 ODS alloy. *Trans Indian Inst Met*, 72: 1395–1398.
<https://doi.org/10.1007/s12666-019-01649-5>
 16. Khalaj O, Mašek B, Jirková H, et al., 2017, Experimental study on thermomechanical properties of new-generation ODS alloys. *Zenodo*, 11: 501–504.
<https://doi.org/10.5281/zenodo.1131439>
 17. Wang G, Huang L, Zhao P, et al., 2020, Effect of heat treatment on microstructure and mechanical properties of ODS nickel-based superalloy via strengthening mechanism. *JOM*, 72: 3279–3287.
<https://doi.org/10.1007/s11837-020-04220-6>
 18. Chun YB, Mao X, Han CH, et al., 2017, Microstructural evolution and tensile properties of oxide dispersion strengthened Alloy 617 at elevated temperatures. *Mater Sci Eng A*, 706: 161–171.
<https://doi.org/10.1016/j.msea.2017.09.009>
 19. Auger MA, Leguey T, Muñoz A, et al., 2011, Microstructure and mechanical properties of ultrafine-grained Fe-14Cr and ODS Fe-14Cr model alloys. *J Nucl Mater*, 417: 213–216.
<https://doi.org/10.1016/j.jnucmat.2010.12.060>
 20. Fintová S, Kuběna I, Luptáková N, et al., 2020, Development of advanced Fe-Al-O ODS alloy microstructure and properties due to heat treatment. *J Mater Res*, 35: 2789–2797.
<https://doi.org/10.1557/jmr.2020.278>
 21. De Sanctis M, Fava A, Lovicu G, et al., 2017, Mechanical characterization of a nano-ODS steel prepared by low-energy mechanical alloying. *Metals (Basel)*, 7: 283.
<https://doi.org/10.3390/met7080283>
 22. Luu DN, Zhou W, Nai SM, 2022, Mitigation of liquation cracking in selective laser melted Inconel 718 through optimization of layer thickness and laser energy density. *J Mater Process Technol*, 299: 117374.
<https://doi.org/10.1016/j.jmatprotec.2021.117374>
 23. Luu DN, Zhou W, Nai SM, 2022, Influence of nano- Y_2O_3 addition on the mechanical properties of selective laser melted Inconel 718. *Mater Sci Eng A*, 845: 143233.
<https://doi.org/10.1016/j.msea.2022.143233>
 24. Yeh AC, Lu KW, Kuo CM, et al., 2011, Effect of serrated grain

- boundaries on the creep property of Inconel 718 superalloy. *Mater Sci Eng A*, 530: 525–529.
- <https://doi.org/10.1016/j.msea.2011.10.014>
25. Deng DW, Wang CG, Liu QQ, et al., 2015, Effect of standard heat treatment on microstructure and properties of borided Inconel 718. *Trans Nonferrous Met Soc China*, 25: 437–443.
- [https://doi.org/10.1016/S1003-6326\(15\)63621-4](https://doi.org/10.1016/S1003-6326(15)63621-4)
26. Zhang Y, Li Z, Nie P, et al., 2013, Effect of heat treatment on niobium segregation of laser-cladded IN718 alloy coating. *Metall Mater Trans A Phys Metall Mater Sci*, 44: 708–716.
- <https://doi.org/10.1007/s11661-012-1459-z>
27. Sui S, Chen J, Ma L, et al., 2019, Microstructures and stress rupture properties of pulse laser repaired Inconel 718 superalloy after different heat treatments. *J Alloys Compd*, 770: 125–135.
- <https://doi.org/10.1016/j.jallcom.2018.08.063>
28. Zhao Y, Li K, Gargani M, et al., 2020, A comparative analysis of Inconel 718 made by additive manufacturing and suction casting: Microstructure evolution in homogenization. *Addit Manuf*, 36: 101404.
- <https://doi.org/10.1016/j.addma.2020.101404>
29. Kumara C, Balachandramurthi AR, Goel S, et al., 2020, Toward a better understanding of phase transformations in additive manufacturing of Alloy 718. *Materialia*, 13: 100862.
- <https://doi.org/10.1016/j.mtla.2020.100862>
30. Mills WJ, 1984, Effect of heat treatment on the tensile and fracture toughness behavior of Alloy 718 weldments. *Weld J*, 63(8): 237s–245s.
31. Cao Y, Bai P, Liu F, et al., 2019, Investigation on the precipitates of IN718 alloy fabricated by selective laser melting. *Metals (Basel)*, 9: 1128.
- <https://doi.org/10.3390/met9101128>
32. Li X, Chu H, Chen Y, et al., 2019, Microstructure and properties of the laser cladding ODS layers on CLAM steel. *Surf Coatings Technol*, 357: 172–179.
- <https://doi.org/10.1016/j.surfcoat.2018.10.006>
33. Guo Y, Li M, Chen C, et al., 2020, Oxide dispersion strengthened FeCoNi concentrated solid-solution alloys synthesized by mechanical alloying. *Intermetallics*, 117: 106674.
- <https://doi.org/10.1016/j.intermet.2019.106674>
34. Shi Y, Lu Z, Yu L, et al., 2020, Microstructure and tensile properties of Zr-containing ODS-FeCrAl alloy fabricated by laser additive manufacturing. *Mater Sci Eng A*, 774: 138937.
- <https://doi.org/10.1016/j.msea.2020.138937>
35. Wilms MB, Streubel R, Frömel F, et al., 2018, Laser additive manufacturing of oxide dispersion strengthened steels using laser-generated nanoparticle-metal composite powders. *Procedia CIRP*, 74: 196–200.
- <https://doi.org/10.1016/j.procir.2018.08.093>
36. Zöllner D, 2022, Impact of a strong temperature gradient on grain growth in films. *Model Simul Mater Sci Eng*, 30: 025010.
- <https://doi.org/10.1088/1361-651X/ac44a8>
37. Rao GA, Kumar M, Srinivas M, et al., 2003, Effect of standard heat treatment on the microstructure and mechanical properties of hot isostatically pressed superalloy Inconel 718. *Mater Sci Eng A*, 355: 114–125.
- [https://doi.org/10.1016/S0921-5093\(03\)00079-0](https://doi.org/10.1016/S0921-5093(03)00079-0)
38. Gladman T, 1999, Precipitation hardening in metals. *Mater Sci Technol*, 15: 30–36.
- <https://doi.org/10.1179/026708399773002782>
39. Sabelkin VP, Cobb GR, Doane BM, et al., 2020, Torsional behavior of additively manufactured nickel alloy 718 under monotonic loading and low cycle fatigue. *Mater Today Commun*, 24: 101256.
- <https://doi.org/10.1016/j.mtcomm.2020.101256>
40. Roper CM, Heczel A, Bhattiprolu VS, et al., 2022, Effect of laser heating on microstructure and deposition properties of cold sprayed SS304L. *Materialia*, 22: 101372.
- <https://doi.org/10.1016/j.mtla.2022.101372>
41. Amato KN, Gaytan SM, Murr LE, et al., 2012, Microstructures and mechanical behavior of Inconel 718 fabricated by selective laser melting. *Acta Mater*, 60: 2229–2239.
- <https://doi.org/10.1016/j.actamat.2011.12.032>
42. Wang Y, Shi J, Deng X, et al., 2012, Contribution of Different Strengthening effects in Particulate-reinforced Metal Matrix Nanocomposites Prepared by Additive Manufacturing. In: Proceeding Advanced Manufacturing. American Society of Mechanical Engineers. Vol. 2; 2016. p1–7. Available from: <https://www.asmedigitalcollection.asme.org/IMECE/proceedings/IMECE2016/50527phoenix,arizona,USA/265241> [Last accessed on 2017 Mar 22].
43. Zhang Z, Chen DL, 2006, Consideration of Orowan strengthening effect in particulate-reinforced metal matrix nanocomposites: A model for predicting their yield strength. *Scr Mater*, 54: 1321–1316.
- <https://doi.org/10.1016/j.scriptamat.2005.12.017>
44. EOS NickelAlloy IN718 Material Data Sheet; 2020.
45. Martienssen W, Warlimont H, 2005, *Springer Handbook of Condensed Matter and Materials Data*. Berlin: Springer.
- <https://doi.org/10.1007/3-540-30437-1>
46. Ferguson JB, Schultz BF, Venugopalan D, et al., 2014, On the superposition of strengthening mechanisms in dispersion strengthened alloys and metal-matrix nanocomposites:

- Considerations of stress and energy. *Met Mater Int*, 20: 375–388.
<https://doi.org/10.1007/s12540-014-2017-6>
47. Ferguson JB, Sheyk-Jaberi F, Kim CS, et al., 2012, On the strength and strain to failure in particle-reinforced magnesium metal-matrix nanocomposites (Mg MMNCs). *Mater Sci Eng A*, 558: 193–204.
<https://doi.org/10.1016/j.msea.2012.07.111>
48. Vogt R, Zhang Z, Li Y, et al., 2009, The absence of thermal expansion mismatch strengthening in nanostructured metal-matrix composites. *Scr Mater*, 61: 1052–1055.
<https://doi.org/10.1016/j.scriptamat.2009.08.025>
49. Nardone VC, Prewo KM, 1986, On the strength of discontinuous silicon carbide reinforced aluminum composites. *Scr Metall*, 20: 43–48.
[https://doi.org/10.1016/0036-9748\(86\)90210-3](https://doi.org/10.1016/0036-9748(86)90210-3)
50. Kim CS, Sohn I, Nezafati M, et al., 2013, Prediction models for the yield strength of particle-reinforced unimodal pure magnesium (Mg) metal matrix nanocomposites (MMNCs). *J Mater Sci*, 48: 4191–4204.
<https://doi.org/10.1007/s10853-013-7232-x>
51. Redsten AM, Klier EM, Brown AM, et al., 1995, Mechanical properties and microstructure of cast oxide-dispersion-strengthened aluminum. *Mater Sci Eng A*, 201: 88–102.
[https://doi.org/10.1016/0921-5093\(94\)09741-0](https://doi.org/10.1016/0921-5093(94)09741-0)
52. Chawla N, Habel U, Shen YL, et al., 2000, The effect of matrix microstructure on the tensile and fatigue behavior of SiC particle-reinforced 2080 Al matrix composites. *Metall Mater Trans A*, 31: 531–540.
<https://doi.org/10.1007/s11661-000-0288-7>
53. Wang S, Zheng Y, Zhang G, et al., 2019, Effect of NbC addition on the microstructure, mechanical properties and thermal shock resistance of Ti(C,N)-based cermets. *Mater Res Express*, 6: 056557.
<https://doi.org/10.1088/2053-1591/ab07e9>
54. Ceschin L, Dahle A, Gupta M, et al., 2017, *Aluminum and Magnesium Metal Matrix Nanocomposites*. Singapore: Springer Singapore.
<https://doi.org/10.1007/978-981-10-2681-2>
55. Patil RV, Kale GB, 1996, Chemical diffusion of niobium in nickel. *J Nucl Mater*, 230: 57–60.
[https://doi.org/10.1016/0022-3115\(96\)80010-9](https://doi.org/10.1016/0022-3115(96)80010-9)
56. Rohrer GS, 1948, Introduction to grains, phases, and interfaces—an interpretation of microstructure. *Metall Mater Trans A Phys Metall Mater Sci*, 175: 15–51.
<https://doi.org/10.1007/s11661-010-0215-5>
57. Cozar R, Pineau A, 1973, Morphology of γ' and γ precipitates and thermal stability of Inconel 718 type alloys. *Metall Trans*, 4: 47–59.
<https://doi.org/10.1007/BF02649604>
58. Burke MG, Miller MK, 2012, Precipitation in Alloy 718: A Combined AEM and APFIM Investigation. Tennessee: Oak Ridge National Laboratory. p337–50.